

Electrical and Electrochemical Behavior of Binary $\text{Li}_4\text{Ti}_5\text{O}_{12}$ –Polyaniline Composite

**M. Khairy, W. A. Bayoumy, K. Faisal,
E. E. Elshereafy & M. A. Mousa**

**Journal of Inorganic and
Organometallic Polymers and
Materials**

ISSN 1574-1443

Volume 30

Number 8

J Inorg Organomet Polym (2020)

30:3158-3169

DOI 10.1007/s10904-020-01478-w

Your article is protected by copyright and all rights are held exclusively by Springer Science+Business Media, LLC, part of Springer Nature. This e-offprint is for personal use only and shall not be self-archived in electronic repositories. If you wish to self-archive your article, please use the accepted manuscript version for posting on your own website. You may further deposit the accepted manuscript version in any repository, provided it is only made publicly available 12 months after official publication or later and provided acknowledgement is given to the original source of publication and a link is inserted to the published article on Springer's website. The link must be accompanied by the following text: "The final publication is available at link.springer.com".



Electrical and Electrochemical Behavior of Binary $\text{Li}_4\text{Ti}_5\text{O}_{12}$ –Polyaniline Composite

M. Khairy^{1,2} · W. A. Bayoumy¹ · K. Faisal³ · E. E. Elshereafy³ · M. A. Mousa¹

Received: 18 November 2019 / Accepted: 18 February 2020 / Published online: 27 February 2020
© Springer Science+Business Media, LLC, part of Springer Nature 2020

Abstract

Polyaniline (PANI), and nanocrystallites of pure $\text{Li}_4\text{Ti}_5\text{O}_{12}$ (LTO) and V-doped $\text{Li}_4\text{Ti}_5\text{O}_{12}$ (V-LTO) spinel structure have been synthesized. The pure and doped $\text{Li}_4\text{Ti}_5\text{O}_{12}$ was synthesized by solid-state reaction, whereas the samples containing PANI were prepared by the in-situ oxidation polymerization method. As-prepared materials were characterized by XRD, FT-IR and SEM techniques. The electrical and electrochemical properties were studied using impedance spectroscopy (EIS), cyclic voltammetry (CV), galvanostatic charge–discharge methods (GCD) techniques. The doping of LTO with vanadium caused marked changes in each of particle size, electrical conductivity, and electrical capacitance without any transforming in the spinel crystal structure of the LTO material. Electrochemical studies showed that the specific capacitance of a hybrid electrode built of the binary materials LTO and PANI is higher than that of its individual single material. It shows a specific capacitance of 108 F/g, an energy density of 30 Wh/kg, and a power density of 2160 W/kg at 4 A/g as well as high cycling performance, with 88.3% capacitance retained over 1000 cycles. The high electrochemical performance of the V-LTO/PANI composite electrode can be attributed to the synergistic effects of the singular constituents and the enhancement of electronic conduction in the hybrid electrode materials.

Keywords Conducting polymers · Composites · Core–shell structure · Energy storage · Supercapacitors

1 Introduction

Among the various realistic solutions, energy can be produced electrochemically and stored in accumulators (batteries) and supercapacitors (SCs) [1–3]. The essential differences between supercapacitors and batteries are in their component materials and the mechanisms concerned in their charge and discharge operations. Batteries have been the technology of choice for most users because they can store considerable quantities of energy in a relatively small volume and weight and deliver proper levels of power for several applications [4–6]. However, the batteries suffer from

several problems such as low-power density and limited charge/discharge cycles. On the other hand, supercapacitors are energy storage devices with very high capacity and a low internal resistance, that can store and produce energy at relatively higher rates as compared to batteries owing to the energy storage mechanism which includes a store charges physically in the electric double layer at a surface-electrolyte interface with much higher power density and no considerable modification in the structure of the material with charge state [7]. The batteries are desired for appliances with high energy density but with limited power output necessitating long-term use of energy while capacitors are favored in purposes where energy is required to be delivered at high power. Owing to their distinct advantages of the supercapacitors (e.g., higher power density, longer cycle life, and better cycle stability), they can be considered as more promising energy storage devices compared with the batteries [8, 9].

In EDLCs, energy is stored via electrostatic accumulation of charges at the electrode–electrolyte interface [10]. In the case of pseudocapacitors, energy is stored by the electrosorption and/or reversible redox reactions at or

✉ K. Faisal
khaled_faisal92@hotmail.com

¹ Chemistry Department, Faculty of Science, Benha University, Banha, Egypt

² Chemistry Department, College of Science, Imam Mohammed Ibn Saud Islamic University, Riyadh, Saudi Arabia

³ Chemistry Department, Faculty of Science, Menoufia University, Shibin Al Kom, Egypt

near the surface of the electrode material, usually a conducting polymer or transition metal [10].

According to their charge storage process, supercapacitors are categorized as either electric double-layer capacitors (EDLCs) or pseudocapacitors [10]. In EDLCs, the energy is stored via the accumulation of charges at the electrode–electrolyte interface reversibly through rapid adsorption–desorption of electrolyte ions. Whereas in pseudocapacitors, energy is stored via fast and reversible Faradaic reactions occurring on the surface of electrode materials such as metal oxides or conducting polymers.

In the energy storage devices, the electrode performance is hugely influenced by its physicochemical properties such as compositional stoichiometry, particle size, crystallinity and morphology of the active material [11, 12]. Among the well-known electrode materials, for high power energy devices, is the inverse spinel- $\text{Li}_4\text{Ti}_5\text{O}_{12}$ (LTO) [13], in which Lithium ions completely occupy tetrahedral 8a sites and 1/6 of the octahedral 16d sites [14]. The other 5/6 of the 16d sites are occupied by titanium-ions, while oxygen fills the 32e tetrahedral sites [14].

The LTO electrode material has several advantages (inexpensive, environmentally friendly, long cycle life, excellent Li-ion mobility, good Li-ion intercalation, and deintercalation reversibility, overcharge resistance, no structural change during the charge–discharge process and wide temperature work range [14]. However, poor electrical conductivity ($\sigma < 10^{-13}$ S/cm) [15], and the sluggish lithium-ion diffusion coefficient (10^{-8} cm²/s) of $\text{Li}_4\text{Ti}_5\text{O}_{12}$ greatly limit its rate performance [16]. Current, numerous tactics have been done to resolve these problems, involving: 1-synthesis of the nanoscale particles to reduce the pathway of Li-ion and in turn increase the diffusion coefficient [13, 17–20]. 2-Surface covering by a conductive phase e.g. by carbon coating [21]. 3-Doping with transition metal ions in the Li^+ -tetrahedral sites or Ti^{4+} -octahedral sites [18, 22–24]. All of these approaches can be also used to improve the intrinsic conductivity of LTO [14, 17, 25–28].

PANI is a well-known conducting polymer for supercapacitor applications due to excellent chemical and thermal stability, good electrical conductivity, high flexibility, low cost, and multi-redox state. It exhibits high theoretical capacitance [29], but its low stability during the charge/discharge process restricts its actual use in supercapacitors [30, 31].

In storage energy devices, the electrode materials prepared from dispersing metal oxides in conducting polymer have drawn a remarkable deal of attention from investigators, because they often exhibit unexpected hybrid properties synergistically derived from both components. In this manner, the hybrid of an electric double-layer material with that of a Faradaic pseudocapacitive material could be a

respectable applicant for a supercapacitor with high energy density and specific capacitance [32–34].

Based on the merits mentioned above, in the present work, we prepared pure LTO and V-doped LTO nanoparticles using the solid-state method as well as PANI and composites of V-LTO/PANI via chemical polymerization method. XRD, FT-IR, SEM, XPS techniques were used for characterizing the samples and electrochemical tools EIS, CV and GCD were applied to investigate the physical characteristics and electrochemical properties of the studied samples. The effect of both doping and surface modification on the electronic conductivity and electrochemical properties of LTO material has been reported and discussed. The V-LTO/PANI composite showed higher specific capacitance and a good cycling life in 1 M LiNO_3 aqueous solution than that of its components.

2 Experimental

2.1 Materials

All chemicals were reagent grade and used without further purification. Lithium carbonate (Li_2CO_3) 98% were purchased from Nice India. Titanium dioxide (TiO_2) 98%, aniline ($\text{C}_6\text{H}_5\text{—NH}_2$) 98.5% were purchased from alpha chemical India. Potassium persulphate ($\text{K}_2\text{S}_2\text{O}_8$) 98%, was purchased from Radel-de Haën Germany. Vanadium pentoxide (V_2O_5) 99% was purchased from Aldrich USA. Poly (vinylidene fluoride) 99.5% was purchased from Sigma-Aldrich France (M. wt = 543,000 g/mol). Hydrochloric acid (HCl) 35% was purchased from dop organik Kimya Turkey. Ethanol ($\text{C}_2\text{H}_5\text{OH}$) 99%. Carbon black was obtained from Alfa Aesar. Fluorine doped tin oxide conducting glass (SnO_2/F) (FTO) with surface resistivity $7 \Omega^2$, transmittance 80–82% visible, and Haze 5% was purchased from Sigma-Aldrich USA.

2.2 Preparation Methods

2.2.1 Preparation of Pure $\text{Li}_4\text{Ti}_5\text{O}_{12}$ (LTO) and V-Doped LTO (V-LTO)

Pure $\text{Li}_4\text{Ti}_5\text{O}_{12}$ (LTO) and V-Doped LTO (V-LTO) were synthesized by a modified solid-state method [35]. They were prepared by mixing starting materials (TiO_2 , Li_2CO_3 , and V_2O_5) using stoichiometric ratios of Li:Ti = 4:5 and 4.6:5 for preparing the LTO(1) and LTO(2) samples, respectively, and Li:Ti:V ratio of 4.55:4.95:0.1 for preparing the V-doped LTO sample. This was followed by ball-milling for a week. The final products of pure and doped (LTO) became ready after heat treating at 760 °C for 2 h under air atmosphere.

2.2.2 Preparation of Polyaniline (PANI)

PANI was synthesized by in-situ oxidation-Polymerization [36]. In the typical procedures, 2 ml of aniline monomer was dissolved in 100 ml of 1 M HCl to form aniline hydrochloride. By using $K_2S_2O_8$ as the oxidant, 50 ml of 0.1 M was dropped wisely with continuous stirring for 3 h in an ice bath. The solution was kept for 24 h to complete polymerization, followed by washing with 200 ml of distilled water to remove the excess of oxidant and unreacted monomers. Finally, the resultant polymer powder was filtrated and obtained after drying at 60 °C for several hours until getting a constant weight of sample. The resultant polymer powder was 1.8 g.

2.2.3 Preparation of Binary System V-LTO / PANI Composite

V-LTO/PANI was prepared with the same polymerization method used for preparing PANI, but in the presence of V-LTO with a mass ratio of V-LTO: Aniline monomer is 1:1.

2.2.4 Materials Characterizations and Measurements

The XRD patterns of the studied materials were recorded by a powder X-ray diffractometer (Philips XL 40) using Cu-K α with $\lambda=0.154$ nm with a diffraction angle between 15° and 80°. The FTIR spectra were taken using an FTIR model Thermo Scientific Nicolet iS10 Spectrometer in the frequency range of 4000–400 cm^{-1} . X-ray Photoelectron Spectroscopy studies were performed using a KRATOS XSAM-800, and calibrated by adventitious carbon.

2.2.5 Electrochemical and Dielectrics Measurements

2.2.5.1 Preparation of Working Electrodes Electrodes were prepared by making a paste of the electrode materials using carbon black and polyvinylidene fluoride with a ratio of 75:15:10, respectively, with few drops of ethanol. The paste was assembled on FTO glass and dried at 80 °C for 2 h to vaporize solvent to achieve the best adhesion on the substrate surface.

2.2.5.2 Electrochemical and Electrical Measurements The energy storage ability of the studied electrodes was assessed by cyclic voltammetry (CV) and galvanostatic charge–discharge (GCD techniques by using (Digi-Ivy 2116 B) instrument, USA. While EIS was measured by (Metrohm auto lab PGSTAT 204), Netherlands at constant potential 10 mV, ranging from 10^{-1} to 10^5 Hz. The standard three-electrode configuration (half-cell) was used to get the electrochemical properties. The prepared materials on FTO were used as working electrodes, saturated calomel electrode (SCE) used as a reference electrode, while Pt foil used as a counter

electrode and 1 M $LiNO_3$ aqueous solution used as the electrolyte. CV was performed between $-1.1:1.1$ V at scan rate 5 mV/s. GCD was measured at a current density of 4 A/g.

AC conductivity (σ_{AC}), Dielectric (ϵ' [dielectric constant], and ϵ'' [dielectric loss]) properties were measured by GW Instek 8110G LCR meter, Taiwan at range 10^3 – 10^7 Hz.

3 Results and Discussions

3.1 Characterizations

XRD patterns of the pure and V- LTO samples are presented in Fig. 1. The pure LTO(1) sample prepared by Li/Ti ratio of 4:5 shows diffraction peaks at $2\theta=18^\circ, 37^\circ, 43^\circ, 49^\circ, 58^\circ, 63^\circ, 66^\circ, 75^\circ, 76^\circ,$ and 79° which correspond to (111), (311), (400), (331), (333), (440), (531), (532), (622), (444) planes, respectively, which are perfectly matched with the cubic spinel phase structure of LTO (JCPDS card no. 49-0207). In addition to the XRD peaks of the spinel phase a rutile TiO_2 impurity phase was also noted at $27^\circ, 41^\circ, 55^\circ,$ and 69° (JCPDS card no. 76-1940), which indicates that not all quantities of TiO_2 reacted with Li_2CO_3 . That's the reason for using the second patch with the Li:Ti ratio of 4.6:5 to prepare pure LTO(2) and Li:Ti:V of 4.55:4.95:0.1 to prepare V- LTO, under the same synthetic conditions used for the first patch. The XRD of the new prepared sample showed the formation of only the LTO spinel structure and the absence of any impurity phases. This matches well with the phase diagram data of TiO_2 – Li_2CO_3 [37]. The XRD of the V-LTO doped sample showed also spinel structure accompanying a slight shift in the diffraction peak to larger θ values than those observed for the pure LTO sample. Moreover, the addition of V into LTO caused an increase in the growth of the crystal through the plane (400) instead of the plane (111). These outcomes point to that the V^{5+} is successfully substituted Ti^{4+} in the spinel lattice structure of $Li_4Ti_5O_{12}$.

The crystallite sizes of LTO specimens were estimated by Scherrer–Debye formula [36] and listed in Table 1, which shows that the crystallite size of V- LTO (89.7 nm) is smaller than that of pure one (116.5 nm). Because $Li_4Ti_5O_{12}$ is face-centered cubic structure, the lattice constant (a) is calculated by using lattice space d_{hkl} according to Eq. (1) [36]

$$d_{hkl} = \frac{a}{\sqrt{(h^2 + k^2 + l^2)}} \quad (1)$$

where (hkl) are the Miller indices. It can be seen that the change in the lattice parameter (a) lies in a parallel way with the change in the ionic radii produced by the individual substitution. Since the ionic radius of V^{5+} is 59.6 pm, which is smaller than Ti^{4+} and Li^+ (68 pm), thus the substitution

Fig. 1 XRD of **a** LTO samples, **b** composite **c** PANI

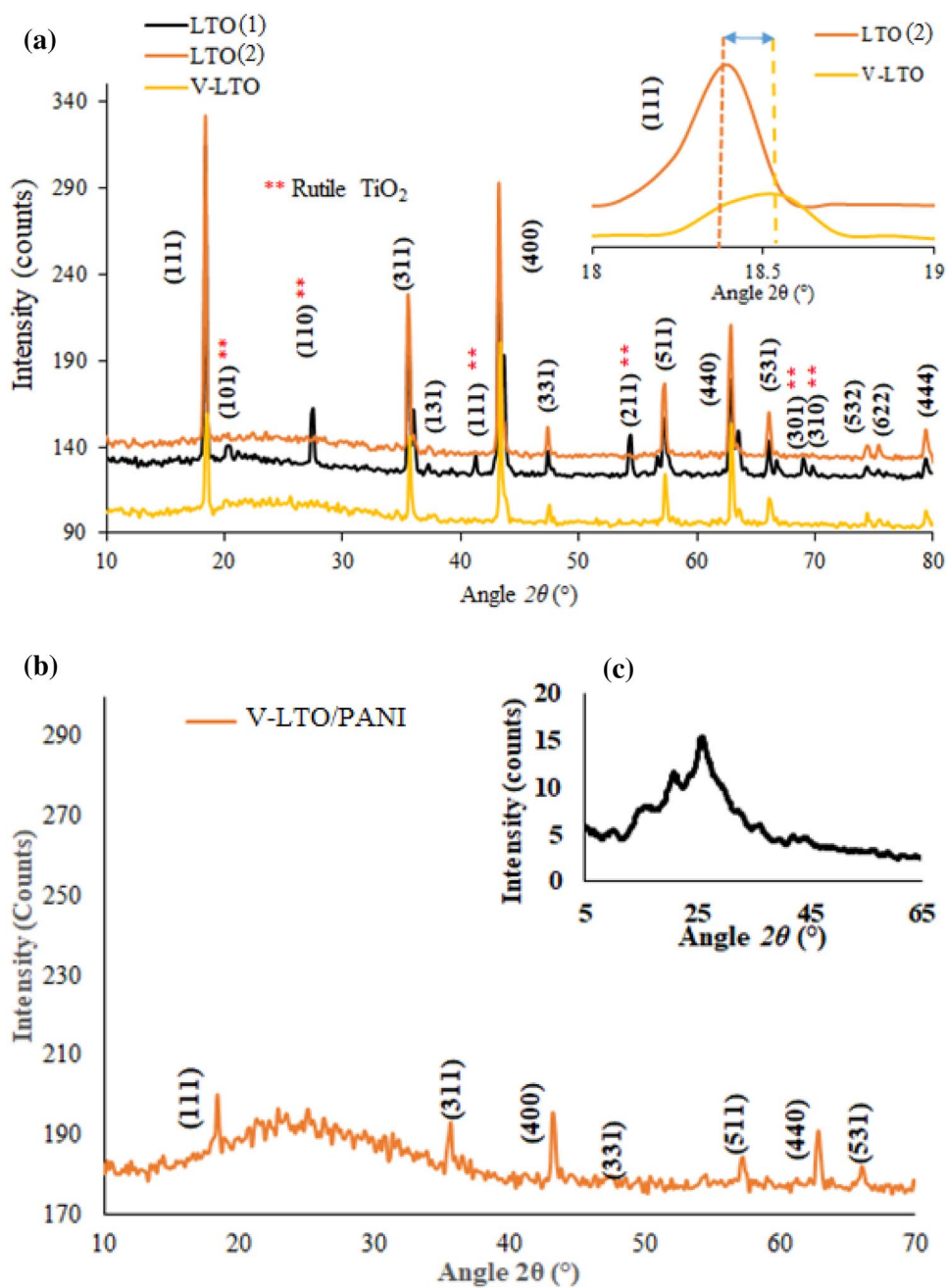


Table 1 XRD, electrical and electrochemical capacitance data of the prepared materials

Sample	C_{sp} (F/g)	Crystal size (nm)	ϵ	Ed (W/kg)	Pd (W/kg)	Cyclability after 1000 cycles (%)	ESR (Ω)	τ (s)	R_{ct} (Ω)
LTO(2)	48(58)	116.5	1.7×10^{-3}	16.1	1757.5	87.2	26	2×10^{-4}	219
V-LTO	76 (72)	89.7	2.6×10^{-3}	20	1800	88.3	27	1.8×10^{-3}	163
PANI	80 (88)	–	–	24.4	2200	81.8	58	3×10^{-4}	22
V-LTO /PANI	92 (108)	–	3.0×10^{-3}	30	2160	88.3	24	4.4×10^{-4}	30

() is C_{sp} from GCD

of Ti^{4+} or Li^+ ions by V^{5+} will lead to decrease in the lattice parameter of LTO crystals as shown in our results; the lattice parameter of V-LTO is 8.336 Å and that of the pure LTO is 8.356 Å.

To clarify the crystalline structures of LTO and V-LTO, besides determining the amount of rutile- TiO_2 in the LTO(1) sample prepared by a Li:Ti ratio of 4:5, a mathematical Rietveld method was applied using the GSAS program with the EXPGUI interface. The obtained results based on a model of Li1 atoms occupying the 8a (1/8, 1/8, 1/8) position, Li2/

Ti atoms occupying the 16d (1/2, 1/2, 1/2) position, and O atoms occupying the 32e (x, x, x) are shown in Fig. 2, and summarized in Table 2, which shows satisfying values for profile (R_p), weighted profile residuals (R_{wp}), and goodness of fit (χ^2). However, some considerable differences in the structure were detected between the three samples (V-LTO and LTO(1) as well as LTO (2) samples prepared by different ratios of Li:Ti). The LTO(1) sample with the ratio of Li:Ti = 4:5 showed a rutile content with 1.54 wt%, and exhibit beside the V-doped LTO, smaller lattice parameter (a), lattice volume (V), oxygen coordinate (x), Li1-O bond distance, and Li1-Li1 bond distance but larger Li2/Ti-O bond distance. These variances point to the existence of larger tetrahedrons and smaller octahedrons in each of the pure LTO and V-doped LTO, and the reverse in LTO(1) containing an impurity of TiO_2 . The number of free octahedral cavities controlled the Li-insertion capacity [38], and the minor value of x recommended lessening structural distortion [20]. Thus, the V-LTO electrode is expected to show a better electrical conductivity and electrochemical functioning compared with both the LTO(1) and LTO(2) electrodes when Li-ion diffuses along the $\langle 011 \rangle$ direction.

Figure 1 b, c shows the XRD of V-LTO/PANI and PANI. A broad peak at $2\theta = 25.5^\circ$, which related the polymer chains of the PANI (Fig. 1c) [37, 39], is also observed for V-LTO/PANI composite sample beside the characteristic peaks of LTO referring to the formation of V-LTO/PANI composite sample. Addition of PANI in composite leads to increase strain (ϵ) on the V-LTO crystal surface.

The strain (ϵ) obtained in our samples was calculated by using Eq. (2) [40], and the results obtained are listed in Table 1.

$$\epsilon = \frac{\beta}{4 \tan \theta} \quad (2)$$

where β is the broadening of diffraction reflection peaks.

Figure 3 shows the FT-IR spectra of the V-LTO, PANI, and their composite. The FT-IR spectrum of PANI demonstrates functional bands locate at 1563, 1475, 1301, 1243, and 1108 cm^{-1} . The bands at 1563 and 1475 cm^{-1} are assigned to the C=C and C=N stretching bands of the quinoid and benzenoid rings, which prove the presence of an oxidized form of PANI (Pernigraniline, PRG) [41]. Bands

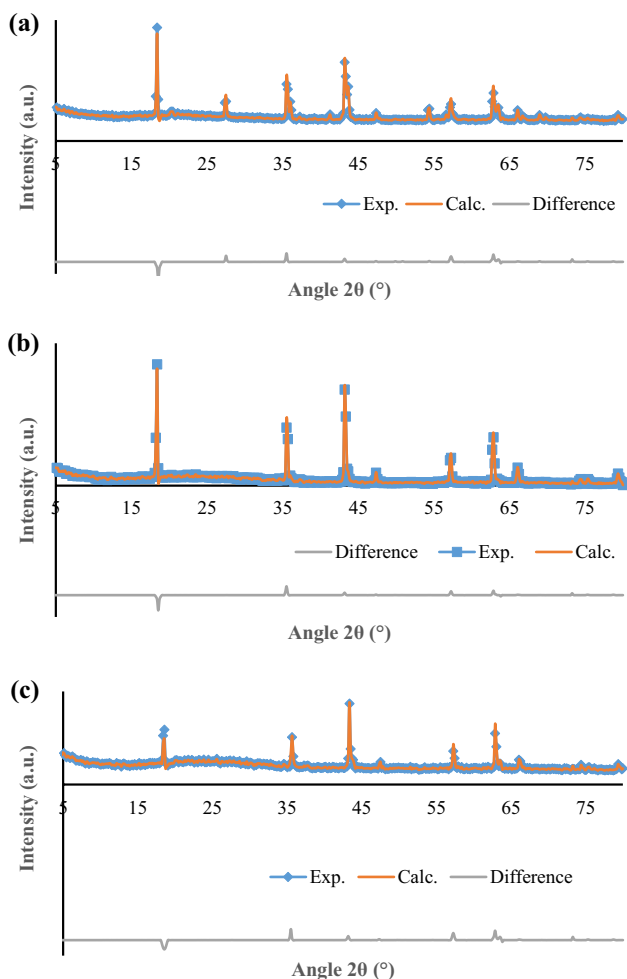


Fig. 2 Rietveld refinement of **a** LTO (1), **b** LTO (2), and **c** V-LTO samples

Table 2 Rietveld refinement data of LTO and V-LTO samples

Sample	a (Å)	V (Å ³)	x	Li1-O (Å)	Li2/Ti-O (Å)	Li1-Li1 (Å)	TiO ₂ (wt%)	R _p (%)	R _{wp} (%)	χ ²
LTO(2)	8.361	584.487	0.2617	1.9734	1.9958	3.6206	–	6.11	7.73	2.223
LTO(1)	8.356	583.439	0.2587	1.9362	2.0186	3.619	1.54	7.41	9.55	2.615
V-LTO	8.336	579.259	0.2554	1.9023	2.0342	3.617	–	8.32	8.56	2.625

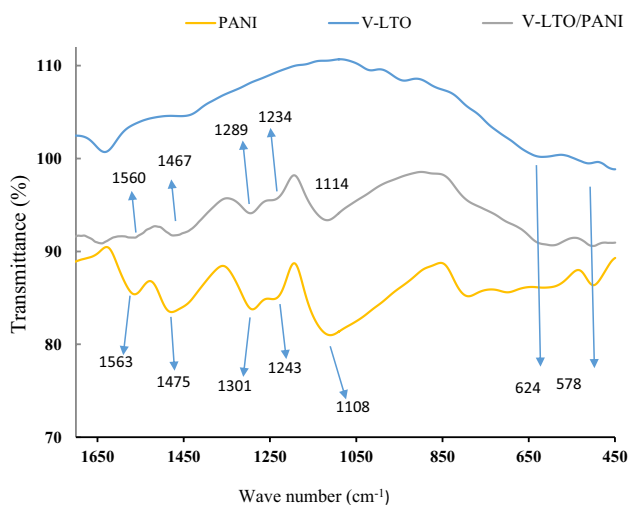


Fig. 3 FT-IR of investigated materials

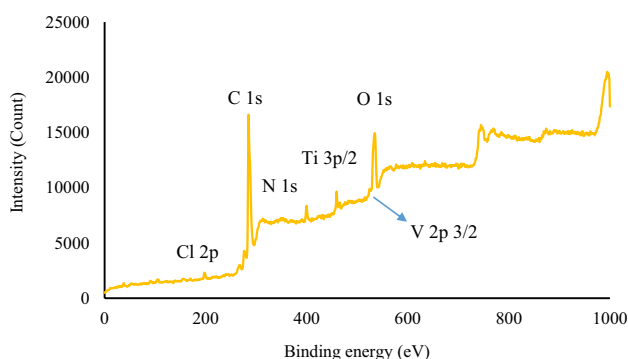


Fig. 4 XPS scan of V-LTO/PANI

at 1301, and 1243 cm^{-1} are related to N–H bending and asymmetric C–N stretching modes of the benzenoid ring, which prove the presence of a reduced form of PANI (emeraldine salt, ES) and indicated that PANI has a half-reduced form (leuco-emeraldine salt, LES) [41]. The band observed at 1108 cm^{-1} is associated with bending vibrational modes of quinonic-type rings referring to the formation of PANI in our sample [42]. The FT-IR spectrum of V-LTO/PANI composite demonstrates two small peaks at 624 and 578 cm^{-1} denoting to Ti–O, and Ti–N vibration, respectively. On comparing the FT-IR spectrum of a composite sample with those of individual constituent, slight shifts in the position of absorption bands are observed, which shows the successful interaction between V-LTO and PANI in their composite [39].

Figure 4 demonstrates the scanner XPS of the V-LTO/PANI sample in binding energy (B.E.) ranges from 0 to 1000 eV. The spectrum shows that the sample contains only the main elements: Ti, O, C, V, Cl, and N suggesting the

formation of the composite. The percentage of C, O, N, Ti, Li, V, and Cl elements was 69.5, 14.8, 9.7, 1.3, 1.1, 0.3, and 3.3%, respectively.

The SEM images of V-LTO, PANI, and their composite are shown in Fig. 5a–c. SEM image of V-LTO (Fig. 5a) shows a cubic morphology with an average length of 0.15 μm . The SEM images of PANI (Fig. 5b) shows clusters of sheets morphology with average grain size of 0.8 μm , while their composite with V-LTO has a core–shell structure of V-LTO with the polymer matrix shell (Fig. 5c) and form agglomerates of size 75 μm , which refers to covering of V-LTO crystals by PANI chains.

3.2 Electrical Studies

AC conductivity (σ_{AC}) of V-LTO, PANI, and their composite was measured at room temperature and frequencies ranged between 10^3 and 10^7 Hz and the results obtained are illustrated in Fig. 6. For all samples, σ_{AC} is almost constant with increasing the frequency until the frequency of $\sim 5 \times 10^5$ Hz, followed by a sharp increase at higher frequencies according to the order: V-LTO/PANI > PANI > LTO > V-LTO. The data obtained are listed in Table 3. This outcome could be explained on the basis of the presence of more interfacial phases in binary system which in turn causes an increase in the polarization of the sample. The results also showed that at all applied frequencies, the σ_{AC} values of LTO are higher than those of V-LTO. This could be explained on the basis that the electronic charge transfer in V-LTO sample, which has a smaller lattice constant than that of LTO, is going to be more scattered through their transfers in the V-LTO lattice [43].

The electrical impedance (EIS) of the investigated samples was measured at frequencies between 10^3 and 10^7 Hz and the data obtained were represented as Cole–Cole plots in Fig. 6. The plots show a single semicircular shaped passing near origin point. This shape is attributed to a parallel combination of grain boundary resistance and grain boundary capacitance of the composite materials. It is interesting to note that the center of each arc lies very close to the real axis, i.e., the angle of dispersion is negligible [44, 45]. The semicircle's center is so close to real axis referring to that composite are electrically homogeneous. The EIS data obtained for all samples are summarized in Table 3. From which it can be seen that the bulk resistance increases in the order:

LTO > V-LTO > V-LTO/PANI > PANI

The effect of frequency on dielectric constant (ϵ'), and dielectric loss (ϵ'') for the investigated materials are represented in Fig. 6. For all samples, the dielectric dispersion was observed where both ϵ' , ϵ'' values reduce fast with raising the frequency in the low-frequency region and approach

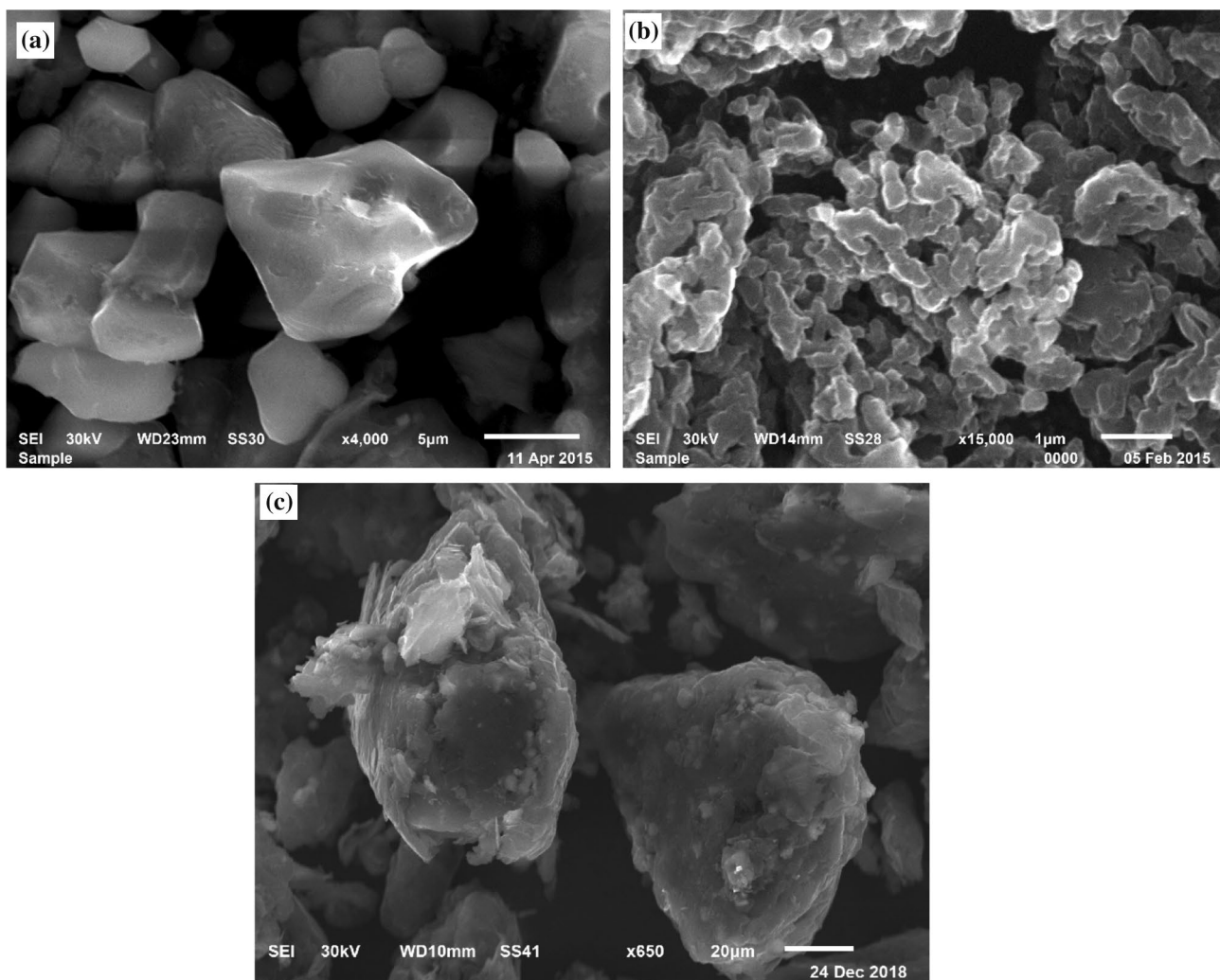


Fig. 5 SEM of **a** V-LTO **b** PANI, and **c** V-LTO/PANI

nearly frequency-independent trend at higher frequencies. This can be explained on the basis of the reduction of the dipoles polarization when the electric field spreads at higher frequencies [46, 47]. It can be also said that, in dielectric nanostructured materials, interfaces with considerable volume fractions hold a large number of defects, such as vacancies, dangling bonds, and micro porosities, which can produce a change in positive and negative space charge distribution at interfaces [48, 49]. Upon applying the electric field, the space charges transfer and when they are caught by defects, a lot of dipole moments are created [50]. At lower frequencies, these dipole moments are simple to track the variation in the electric field. Consequently, the dielectric loss and so the dielectric constant exhibits a large value at low frequency as listed in Table 3.

3.3 Electrochemical Studies

CV is a suitable technique to show types of capacitive mechanisms. Figure 7 shows CV for the prepared electrodes at a scanning rate of 5 mV/s. CV plots of LTO, V-LTO, and PANI clearly show different electrochemical behavior, where redox peaks observed in the curves are due to oxidation and reduction of active sites at the electrode [51, 52]. The redox peaks seen in CV of PANI are attributed to $LES \leftrightarrow ES \leftrightarrow PRG$ transformations, respectively [53, 54]. Whereas, The CV of LTO electrode, Fig. 7, shows redox peaks at -0.08 V, and -0.2 V referring to Ti^{4+}/Ti^{3+} redox process. The redox peaks of V-LTO are slightly shifted comparable with those of LTO electrode. The Cyclic voltammograms of V-LTO/PANI composite represented in Fig. 7,

Fig. 6 Effect of frequency on electrical properties of LTO(2), PANI, V-LTO and PANI/V-LTO doped samples

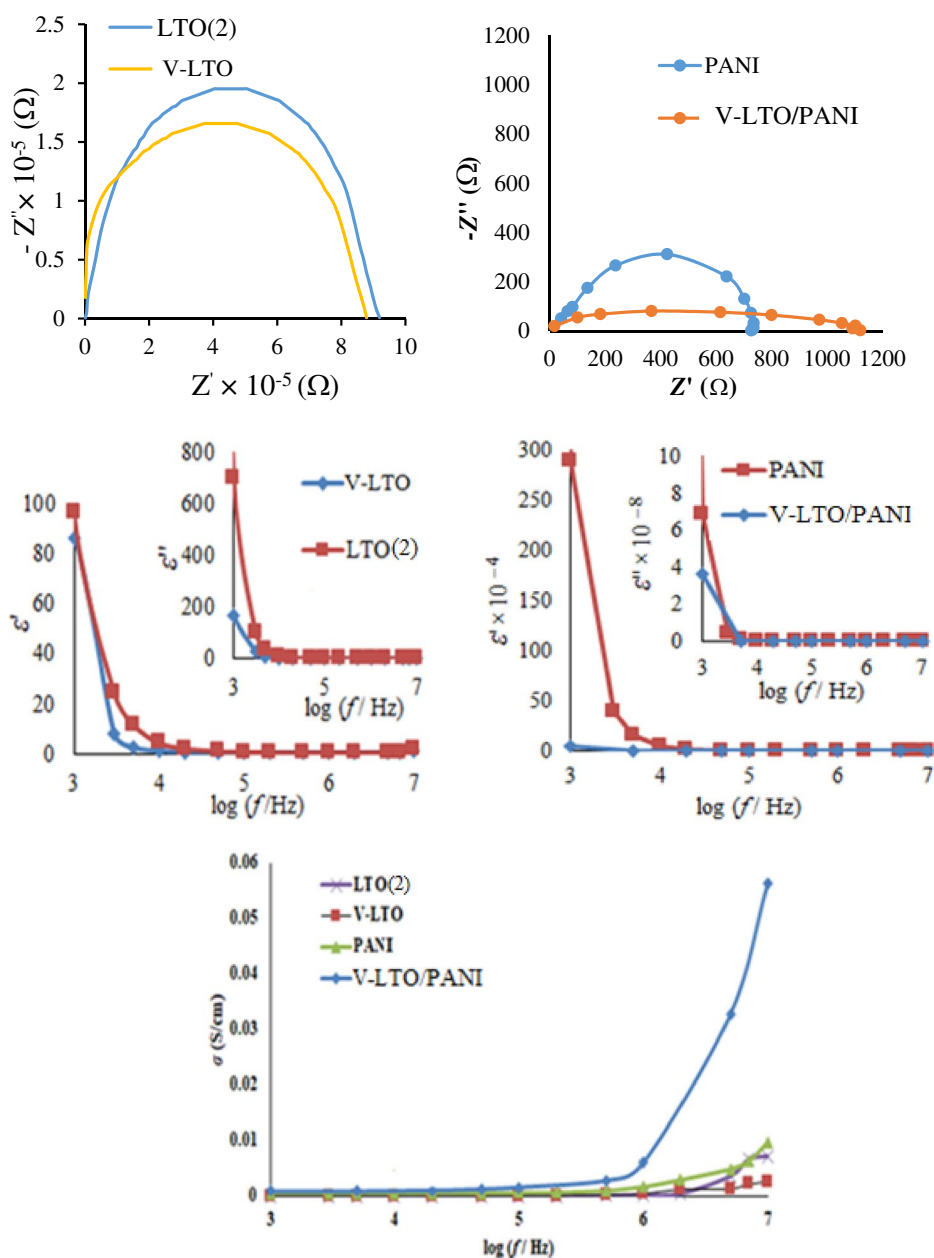


Table 3 Electrical conductivity and dielectric data of the prepared materials

Sample	1000 Hz			500 kHz			10 MHz			R_b (Ω)
	σ (S/cm)	ϵ'	ϵ''	σ (S/cm)	ϵ'	ϵ''	σ (S/cm)	ϵ'	ϵ''	
LTO(2)	7.3×10^{-7}	0.96×10^2	7.0×10^2	5.5×10^{-5}	2.1	1.1×10^{-2}	7×10^{-4}	2.0	333×10^{-3}	9.19×10^5
V-LTO	3.4×10^{-7}	0.91×10^2	1.6×10^2	5.0×10^{-5}	1.56	1.2×10^{-2}	3×10^{-4}	1.5	332×10^{-3}	8.78×10^5
PANI	8.1×10^{-4}	3.01×10^6	7.1×10^8	9.1×10^{-4}	4.6×10^1	6.2×10^1	9×10^{-3}	13.8	1.10×10^1	6.85×10^2
V-LTO /PANI	9.1×10^{-4}	6.03×10^4	4.2×10^8	2.8×10^{-3}	3.2	2.8	5.6×10^{-2}	1.8	0.1	1.10×10^3

shows the same previously mentioned peaks for PANI and LTO with slight shift ranged ± 0.01 V, which attributed to the change occurring in the composite structure due to

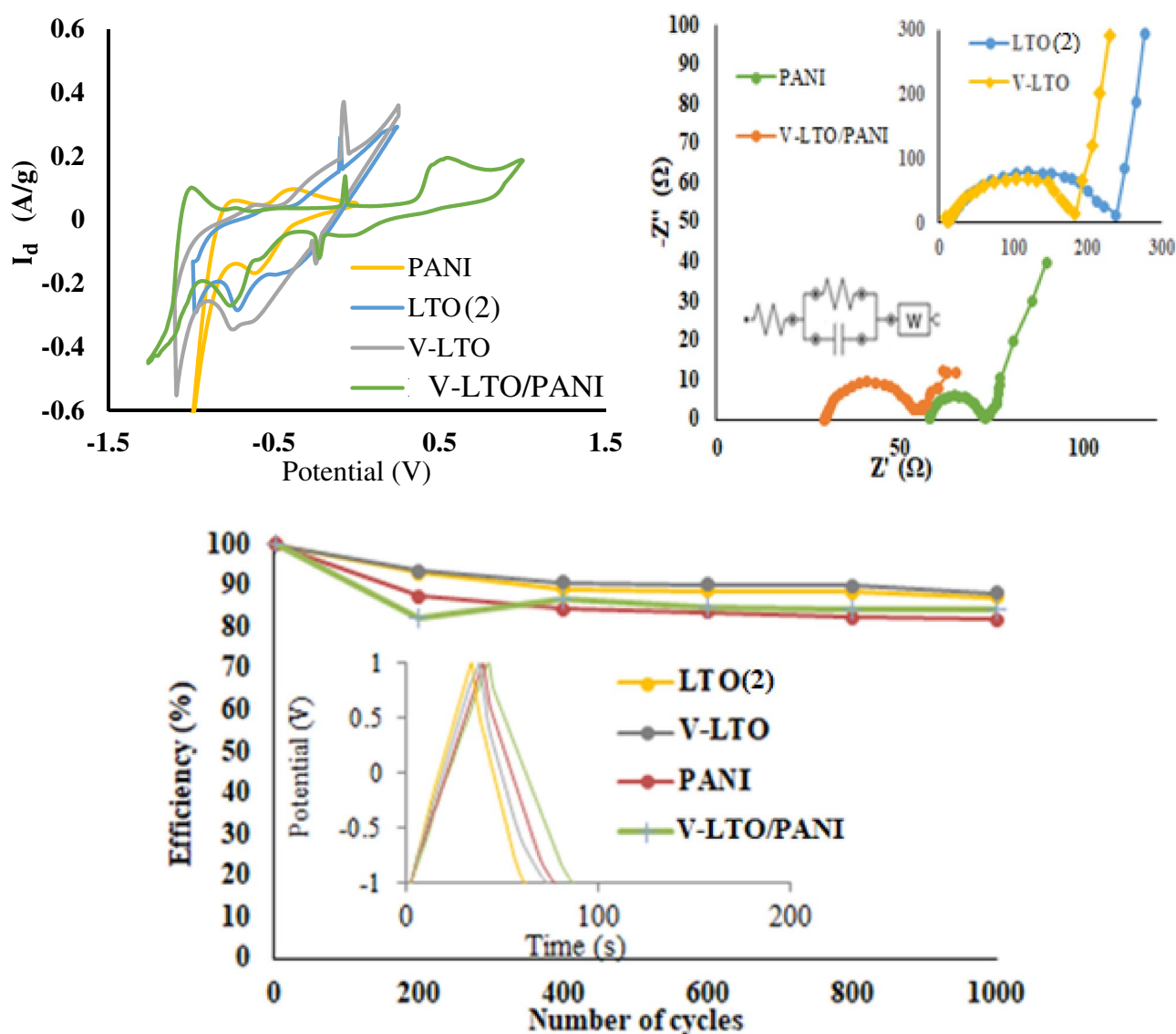


Fig. 7 CV, EIS, and GCD of the investigated electrodes in 1 M aq. LiNO₃

interaction performing between V-LTO, and PANI. The specific capacitance (C_{sp}) values of all the electrodes studied were calculated from CV data by using Eq. (3) [55] and listed in Table 1.

$$C_{sp} = \frac{1}{m\nu\Delta V} \int_{-V}^{+V} IV\partial V \quad (3)$$

where I is current (A), V is applied potential (V), ν is scan rate (V/s), and m is mass of active material (g).

Galvanostatic charging–discharging (GCD) is a complementary technique for determining the C_{sp} of electrochemical capacitors at constant current. Therefore, the electrochemical operations of the electrode materials were also investigated by galvanostatic charge/discharge measurements

at a current density of 4 A/g and the results obtained are illustrated in Fig. 7. All discharge curves displayed an internal resistance drop (IR-drop), which realized as the equivalent series resistance (ESR) that involves both electrode and electrolyte resistances, besides the contact resistance among the electrodes, separator, and the electrolyte. The discharge curves of the composite electrode demonstrate a departure from a straight line owing to their pseudocapacitive nature. The specific capacitance of the electrodes (C_{sp}) was calculated from the discharge cycles using Eq. (4) [56].

$$C_{sp} = \frac{1\Delta t}{m\Delta V} \quad (4)$$

where I is the response current density, Δt is the discharge time, m is the mass of the active materials on the electrode,

and ΔV is the potential range during the charge–discharge measurement. The results obtained are given in Table 1, which shows that the capacity increases according to V-LTO/PANI > PANI > V-LTO > LTO. These agree well with those obtained from CV results. The increase in the capacitance of V-LTO compared with that of LTO is attributed to decreasing the particle size of the doped sample, which leads to fast Li-ion diffusion because of the shorted Li-ion path and widened electrode/electrolyte contact surface [57]. Moreover, a reduction in the internal resistance (IR) was detected denoting the decrease in the resistance of the electrode.

Long cycling stability is an important parameter for supercapacitor operations. Thus, the electrochemical stability of the examined electrodes was investigated, at a current density of 4 A/g. The outcomes obtained are shown in Fig. 7, and summarized in Table 1, which shows that after 1000 cycles the stability of the electrodes has the order: V-LTO/PANI > LTO > V-LTO > PANI and lie in the range of 81–94% of their initial capacitances.

The Nyquist plots of investigated electrodes over a frequency range of 0.01 Hz to 100 kHz are illustrated in Fig. 7. At higher frequencies, the intersection built on the Z' -axis of the Nyquist plot shows the solution resistance (R_s). At medium frequency region, one depressed semicircle was monitored [58], which is associated with the surface property of the electrode resultant from the charge transfer resistance (R_{ct}) at the electrode/electrolyte interface. Moreover, at the lower frequencies, a spike was observed revealing the supercapacitor behavior. The spike stands for the Warburg impedance (W) of the electrode, i.e., the diffusive resistance of Li^+ ions into electrode [27, 59]. For understanding the charge transfer process at the electrolyte–electrode interface, the semicircle observed at the higher frequencies is magnified and the R_{ct} -value at the electrolyte–electrode interface is determined by extrapolation of the semicircle on the real impedance axis and determine the diameter of the semi-circle, which represents the charge transfer resistance R_{ct} . The results obtained are given in Table 1, which shows R_{ct} follows the order: LTO > V-LTO > V-LTO/PANI > PANI.

The equivalent series resistance, ESR, was determined in the high-frequency region from the first intersection point on the Z' -axis and found to be: 26, 27, 24 and 58 Ω , for LTO, V-LTO, V-LTO/PANI, and PANI, respectively. The difference in ESR-value can be attributed to the diverse conductivities of electrode materials because it is attributed to the intrinsic resistance of the active material, the electrolyte resistance, and the active material/current collector interface.

The time constants (τ) of the capacitors were calculated from the frequency (f) matching at the maximum of the semicircle using Eq. (5) [60] and the results obtained are listed in Table 1:

$$\tau = \frac{1}{f} \quad (5)$$

The τ value increases in the order: V-LTO > V-LTO/PANI > PANI > LTO. The small-time constants of the binary system reveal tits high power response [38]

In order to determine the electrochemical performance of the binary system electrode (V-LTO/PANI, has highest C_{sp}) the power (P_d) and the energy density (E_d) were calculated by Eqs. (6, 7) [56]:

$$E_d = \frac{1}{2} C \Delta V^2 \quad (6)$$

$$P_d = \frac{E_d}{t} \quad (7)$$

where ΔV is the voltage change during the discharging time t after IR drop. The energy density and power density are found to be 30 Wh/kg and 2160 W/kg, respectively.

4 Conclusions

In conclusion, pure, and V^{+5} doped LTO spinel nanoparticles were prepared using a solid-state reaction method in air atmosphere, and polyaniline was synthesized by chemical polymerization. The vanadium doping onto Ti sites did not cause any change in the crystal structure, but it decreases each of lattice parameters, particle size, and electrical conductivity. The decrease in particle size by V-doping leading to the improved specific surface area and shortened Li+ transfer path, which in turn efficiently enhance the electrochemical performance of LTO. Electrical conductivity, dielectric constant and electrochemical behavior of PANI, V-LTO/PANI composite were investigated and compared with the corresponding behavior of pure LTO. The electrochemical functioning was studied by using CV and GCD techniques. The data obtained showed that V-LTO has a higher specific capacity than that of pristine LTO. Moreover, the as-prepared binary electrode (V-LTO/PANI) exhibits much higher specific capacitance than the two individual components. The composite electrode exhibits a specific capacitance of 108 F/g, an energy density of 30 Wh/kg and a power density of 2160 W/kg, and good cycling performance, with 88.2% capacitance retained over 1000 cycles. This work reveals that composite electrodes of doped LTO materials are useful for application in energy storing.

References

1. D. Chao et al., Graphene quantum dots coated VO_2 arrays for highly durable electrodes for Li and Na ion batteries. *Nano Lett.* **15**, 565–573 (2014)

- M. Chen et al., Rapid pseudocapacitive sodium-ion response induced by 2D ultrathin tin monoxide nanoarrays. *Adv. Funct. Mater.* **27**, 160–172 (2017)
- Z. Liu et al., Nano energy towards wearable electronic devices: a quasi-solid-state aqueous lithium-ion battery with outstanding stability, flexibility, safety and breathability. *Nano Energy* **44**, 164–173 (2018)
- J. Duay, M. Kelly, T.N. Lambert, Evaluation of a ceramic separator for use in rechargeable alkaline Zn/MnO₂ batteries. *J. Power Sources* **395**, 430–438 (2018)
- D. Zhao, Y. Wang, Y. Zhang, High-performance Li-ion batteries and super-capacitors based on 1-D. *Nano-Micro Lett.* **3**, 62–71 (2011)
- M.D. Stoller, S. Park, Y. Zhu, J. An, R.S. Ruoff, Graphene-based ultracapacitors. *Nano Lett.* **8**, 3498–3502 (2008)
- J. Zhou et al., A conductive and highly deformable all-pseudocapacitive composite paper as supercapacitor electrode with improved areal and volumetric capacitance. *Small* **14**, 1803–1816 (2018)
- A. Elmouwahidi, E. Bailón-garcía, A.F. Pérez-cadenas, N. Fernández-sáez, F. Carrasco-marín, Development of vanadium-coated carbon microspheres: electrochemical behavior as electrodes for supercapacitors. *Adv. Funct. Mater.* **28**, 1802–1817 (2018)
- X. Liu, D. Li, X. Chen, W. Lai, W. Huang, Highly transparent and flexible all-solid-state supercapacitors based on ultra-long silver nanowire conductive networks. *Appl. Mater. Interfaces* **10**, 32536–32542 (2018)
- P. Simon, Y. Gogotsi, Materials for electrochemical capacitors. *Nat. Mater.* **7**, 845–854 (2008)
- Y.S. Lee, Y.K. Sun, K.S. Nahm, Synthesis of spinel LiMn₂O₄ cathode material prepared by an adipic acid-assisted sol-gel method for lithium secondary batteries. *Solid State Ionics* **109**, 285–294 (1998)
- B.J. Hwang, C.Y. Wang, M.Y. Cheng, R. Santhanam, Structure, morphology, and electrochemical investigation of LiMn₂O₄ thin film cathodes deposited by radio frequency sputtering for lithium microbatteries. *J. Phys. Chem. C* **113**, 11373–11380 (2009)
- F. Li, M. Zeng, J. Li, H. Xu, Preparation and electrochemical performance of Mg-doped Li₄Ti₅O₁₂ nanoparticles as anode materials for lithium-ion batteries. *Int. J. Electrochem. Sci.* **10**, 10445–10453 (2015)
- B. Lee, J.R. Yoon, Preparation and characteristics of Li₄Ti₅O₁₂ with various dopants as anode electrode for hybrid supercapacitor. *Curr. Appl. Phys.* **13**, 1350–1353 (2013)
- T. Yi et al., Spinel Li₄Ti_{5-x}Zr_xO₁₂ (0 ≤ x ≤ 0.25) materials as high-performance anode materials for lithium-ion batteries. *J. Alloys Compd.* **558**, 11–17 (2013)
- H. Jung, N. Venugopal, B. Scrosati, Y. Sun, A high energy and power density hybrid supercapacitor based on an advanced. *J. Power Sources* **221**, 266–271 (2013)
- H. Yu et al., High-rate characteristics of novel anode Li₄Ti₅O₁₂/polyacene materials for Li-ion secondary batteries. *Electrochim. Acta* **53**, 4200–4204 (2008)
- K. Mukai, K. Ariyoshi, T. Ohzuku, Comparative study of Li[CrTi]O₄, Li[Li_{1/3}Ti_{5/3}]O₄ and Li_{1/2}Fe_{1/2}[Li_{1/2}Fe_{1/2}Ti]O₄ in non-aqueous lithium cells. *J. Power Sources* **146**, 213–216 (2005)
- R. Bernhard, S. Meini, H.A. Gasteiger, On-line electrochemical mass spectrometry investigations on the gassing behavior of Li₄Ti₅O₁₂ electrodes and its origins. *J. Electrochem. Soc.* **161**, A497–A505 (2014)
- H. Song et al., An upper limit of Cr-doping level to retain zero-strain characteristics of Li₄Ti₅O₁₂ anode material for li-ion batteries. *Sci. Rep.* **7**, 43335 (2017)
- E. Zhang, H. Zhang, Preparation and electrochemical properties of carbon-coated Li₄Ti₅O₁₂ anode materials for lithium ion batteries. *Int. J. Electrochem. Sci.* **13**, 12380–12390 (2018)
- X. Li, M. Qu, Z. Yu, Structural and electrochemical performances of Li₄Ti_{5-x}Zr_xO₁₂ as anode material for lithium-ion batteries. *J. Alloys Compd.* **487**, 12–17 (2009)
- B.G. Lee, J.R. Yoon, Preparation and characteristics of Li₄Ti₅O₁₂ anode material for hybrid supercapacitor. *J. Electron. Eng. Technol.* **7**, 207–211 (2012)
- E. Kang et al., Highly improved rate capability for a lithium-ion battery nano- Li₄Ti₅O₁₂ negative electrode via carbon-coated mesoporous uniform pores with a simple self-assembly method. *Adv. Funct. Mater.* **21**, 4349–4357 (2011)
- L. Yang, L. Gao, Li₄Ti₅O₁₂/C composite electrode material synthesized involving conductive carbon precursor for Li-ion battery. *J. Alloys Compd.* **485**, 93–97 (2009)
- H. Narayan, H. Alemu, E. Iwuoha, Synthesis, characterization and conductivity measurements of polyaniline and poly aniline/fly-ash composites. *Phys. Status Solidi Appl. Mater. Sci.* **203**, 3665–3672 (2006)
- S.K. Meher, P. Justin, G.R. Rao, Microwave-mediated synthesis for improved morphology and pseudocapacitance performance of nickel oxide. *ACS Appl. Mater. Interfaces* **3**, 2063–2073 (2011)
- M. Chen, W. Li, X. Shen, G. Diao, Fabrication of core-shell α-Fe₂O₃ @ Li₄Ti₅O₁₂ composite and its application in the lithium ion batteries. *ACS Appl. Mater. Interfaces* **6**, 4514–4523 (2014)
- C. Gomez-Navarro et al., Electronic transport properties of individually chemically reduced graphene oxide sheets. *Nano Lett.* **7**, 3499–3503 (2007)
- R. Dominko, M. Gaberscek, M. Bele, D. Mihailovic, J. Jamnik, Carbon nanocoatings on active materials for Li-ion batteries. *J. Eur. Ceram. Soc.* **27**, 909–913 (2007)
- Q. Wu, Y. Xu, Z. Yao, A. Liu, G. Shi, Supercapacitors based on flexible graphene/polyaniline nanofiber composite films. *ACS Nano* **4**, 1963–1970 (2010)
- A.S. Adekunle, K.I. Ozoemena, Electron transfer behaviour of single-walled carbon nanotubes electro-decorated with nickel and nickel oxide layers. *Electrochim. Acta* **53**, 5774–5782 (2008)
- A.S. Adekunle, K.I. Ozoemena, Insights into the electro-oxidation of hydrazine at single-walled carbon-nanotube-modified edge-plane pyrolytic graphite electrodes electro-decorated with metal and metal oxide films. *J. Solid State Electrochem.* **12**, 1325–1336 (2008)
- R. Younesi, G.M. Veith, P. Johansson, K. Edström, T. Vegge, Lithium salts for advanced lithium batteries: Li-metal, Li-O₂, and Li-S. *Energy Environ. Sci.* **8**, 1905–1922 (2015)
- M. Khairy, K. Faisal, M.A. Mousa, High-performance hybrid supercapacitor based on pure and doped Li₄Ti₅O₁₂ and graphene. *J. Solid State Electrochem.* **21**, 873–882 (2017)
- Z. Durmus, A. Baykal, H. Kavas, H. Szeri, Preparation and characterization of polyaniline (PANI)/Mn₃O₄ nanocomposite. *Phys B* **406**, 1114–1120 (2011)
- A. Laumann, Novel routes to Li₄Ti₅O₁₂ spinel: characterization and phase relations. Thesis, Fakultät für Geowissenschaften der Ludwig Maximilians, München University, Germany **1**, 1–164 (2010)
- H. Ge, N. Li, D. Li, C. Dai, D. Wang, Study on the theoretical capacity of spinel lithium titanate induced by low-potential intercalation. *J. Phys. Chem. C* **113**, 6324–6326 (2009)
- A. Gabal et al., Synthesis, characterization and electrical conductivity of polyaniline-Mn_{0.8}Zn_{0.2}Fe₂O₄ nano-composites. *Int. J. Electrochem. Sci.* **11**, 4526–4538 (2016)
- N. Ahmed, M. Ramadan, W.M.A. El, Non-precious co-catalysts boost the performance of TiO₂ hierarchical hollow mesoporous spheres in solar fuel cells. *Int. J. Hydrog. Energy* **43**, 21219–21230 (2018)
- Z.G. Bellal et al., Synthesis and electrical conducting properties of poly(aniline) doped with zeolite HY nanocomposites containing

- SnO₂ for high-performance supercapacitor electrode. *J. Inorg. Organomet. Polym. Mater.* **29**, 1548–1558 (2019)
42. V.J. Babu, S. Vempati, S. Ramakrishna, Conducting polyaniline-electrical charge transportation. *Mater. Sci. Appl.* **4**, 1–10 (2013)
 43. S. Ganapathy, M. Wagemaker, Nanosize storage properties in spinel Li₄Ti₅O₁₂ explained by anisotropic surface lithium insertion. *ACS Nano* **6**, 8702–8712 (2012)
 44. S.M. Ebrahim, Fabrication of Schottky diode based on Zn electrode and polyaniline doped with 2-acrylamido-2-methyl-1-propanesulfonic acid sodium salt. *J. Polym. Res.* **16**, 481–487 (2009)
 45. A.S. Roy, S.G. Hegde, A. Parveen, Synthesis, characterization, AC conductivity, and diode properties of polyaniline-CaTiO₃ composites. *Polym. Adv. Technol.* **25**, 130–135 (2014)
 46. M. Khairy, M.A. Mousa, nanoparticles. *Int. J. Mater. Chem.* **2**, 197–204 (2013)
 47. M. Wilkening, R. Amade, W. Iwaniak, P. Heitjans, Ultraslow Li diffusion in spinel-type structured Li₄Ti₅O₁₂—A comparison of results from solid state NMR and impedance spectroscopy. *Phys. Chem. Chem. Phys.* **9**, 1239–1246 (2007)
 48. Z. Li, J. Li, Y. Zhao, K. Yang, F. Gao, X. Li, Structure and electrochemical properties of Sm-doped Li₄Ti₅O₁₂ as anode material for lithium-ion batteries. *RSC Adv.* **6**, 15492–15500 (2016)
 49. Y.P. Al et al., Synthesis of Li₄Ti₅O₁₂-Sn by ultrasonic method as anode materials for lithium ion battery. *IOP Conf. Ser. Mater. Sci. Eng.* **432**, 432 (2018)
 50. Ü.A. Bilgin et al., Optical and dielectric properties of PMMA/ α -Fe₂O₃-ZnO nanocomposite films. *J. Inorg. Organomet. Polym. Mater.* **29**, 1514–1522 (2019)
 51. Z.Y. Yang et al., Controllable growth of CNTs on graphene as high-performance electrode material for supercapacitors. *ACS Appl. Mater. Interfaces* **6**, 8497–8504 (2014)
 52. S. Hong, X. Huang, H. Liu, Z. Gao, In situ chemical synthesis of MnO₂/HMCNT nanocomposite with a uniquely developed three-dimensional open porous architecture for supercapacitors. *J. Inorg. Organomet. Polym. Mater.* **29**, 1587–15960 (2019)
 53. L. Wang et al., Hierarchical nanocomposites of polyaniline nanowire arrays on reduced graphene oxide sheets for supercapacitors. *Sci. Rep.* **3**, 1–9 (2013)
 54. Z. Neisi, Z. Ansari-Asl, A.S. Dezfuli, Polyaniline/Cu(II) metal-organic frameworks composite for high performance supercapacitor electrode. *J. Inorg. Organomet. Polym. Mater.* **29**, 1838–1847 (2019)
 55. M. Ciszewski, A. Mianowski, P. Szatkowski, G. Nawrat, J. Adamek, Reduced graphene oxide-bismuth oxide composite as electrode material for supercapacitors. *Ionics (Kiel)*. **21**, 557–563 (2014)
 56. M.A. Mousa, M. Khairy, M. Shehab, Nanostructured ferrite/graphene/ polyaniline using for supercapacitor to enhance the capacitive behavior. *J. Solid State Electrochem.* **21**, 995–1005 (2017)
 57. E. Pohjalainen, T. Rauhala, M. Valkeapa, J. Kallioinen, T. Kallio, Effect of Li₄Ti₅O₁₂ particle size on the performance of lithium ion battery electrodes at high C—rates and low temperatures. *J. phy. Chem. C* **119**, 2277–2283 (2015)
 58. S. Kim et al., Reduced graphene oxide/ZnO nanorods nanocomposite: structural, electrical and electrochemical properties. *J. Inorg. Organomet. Polym. Mater.* **29**, 2282–2290 (2019)
 59. H. Xia, W. Xiao, M.O. Lai, L. Lu, Facile synthesis of novel nanostructured MnO₂ thin films and their application in supercapacitors. *Nanoscale Res. Lett.* **4**, 1035–1040 (2009)
 60. M. Zhi, C. Xiang, J. Li, M. Li, N. Wu, Nanostructured carbon—metal oxide composite electrodes for supercapacitors : a review. *Nanoscale* **5**, 72–88 (2013)

Publisher's Note Springer Nature remains neutral with regard to jurisdictional claims in published maps and institutional affiliations.